Nanoscale

Accepted Manuscript

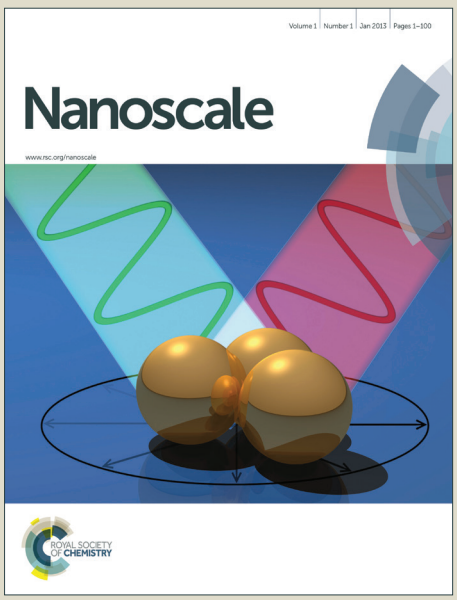

ROYAL SOCIETY OF CHEMISTRY

www.rsc.org/nanoscale

Journal Name

RSCPublishing

ARTICLE

Hollow manganese phosphonate microspheres with hierarchical porosity for efficient adsorption and separation

Cite this: DOI: 10.1039/x0xx00000x

Yun-Pei Zhu,[a] Ya-Lu Liu,[a] Tie-Zhen Ren[b] and Zhong-Yong Yuan*[a]

Received 00th January 2012,
Accepted 00th January 2012

DOI: 10.1039/x0xx00000x

www.rsc.org/

Hollow manganese phosphonate microspheres of inorganic-organic hybrid with hierarchically porous shells were prepared through a template-free hydrothermal method using ethylene diamine tetra(methylene phosphonic acid) as the coupling molecule. The hollow structures with hierarchical porosity were confirmed by SEM, TEM and N_2 sorption. FT-IR, XPS and TG-DSC measurements revealed that the organophosphonate linkers were homogeneously incorporated into the hybrid framework. The hierarchical manganese phosphonates could be used as efficient adsorbents for the removal of copper ions, showing fast binding kinetics due to the well-structured porosity. The adsorption process follows pseudo-second order reaction kinetics, as well as Langmuir isotherm, indicating that Cu^{2+} was monolayer adsorbed on the hybrid by chemical complexation. Furthermore, the synthesized manganese phosphonates with peculiar porosity exhibited excellent size selectivity for protein adsorption in a complex solution, presenting the promising potential as candidates for biomaterials.

1. Introduction

Nanomaterials with the similar composition but distinct morphologies present substantially different physical, chemical and mechanical properties. Some typical examples are nanoparticles, nanowires, nanorods, hollow materials, nanotubes, and many other unique structures.[1-4] Among the various unique structures, hollow nanomaterials have received much research interest due to their special properties including large fractional void space, large specific surface area, low density, and tunable refractive index.[5-8] Their potential applications have extended to catalysis, photonic crystals, enzyme immobilization, and biomedical diagnosis and therapy.[9-11] The usual strategies for the preparation of hollow materials can be classified into interior-templating method relating to the utilization of soft/hard templates and template-free route.[12] The templates for the synthesis of hollow include polystyrene latex spheres,[13] silica sols,[14] vesicles,[15] polymer micelles,[16] microemulsion droplets.[17] However, although templating method is efficient and general, the further removal of the templates not only perplexes the fabrication procedures, but also may result in the collapse of the hollow structures, and even detrimentally introduce some impurities. For this regard, significant attention has been directed to template-free method for generating hollow micro- and nanostructures involving metastable Kirkendall effect,[18] Ostwald ripening,[19] chemically induced self-transformation,[20] and anion-exchange reactions.[21] Template-free method appears to be particularly significant for constructing hollow microstructured spheres with complex internal and external textures.[22] Nevertheless, most of the previously reported template-free approaches are time- and energy-consuming or require multi-step processes. Therefore, the development of simple and fast methods to prepare hollow structures still remains a challenge.

Rational design of novel nanoporous materials with well-structured network topologies is one of the most significant and challenging fields of research due to the extensive potentials in sensing, catalysis, gas adsorption, and sensitized solar cells.[23] In comparison with inorganic materials, chemically designed organic-inorganic hybrids can be considered as nanocomposites in which the organic and inorganic components are intimately mixed on a molecular level, showing combined superiorities of organic moieties and inorganic units.[24-26] However the conventional nanoporous organosiliceous materials present difficulties in wide practical application due to the limited choice and high cost of the organosilicane precursors. The exploitation of porous hybrid materials has thus been extended to non-silica-based inorganic–organic hybrid materials.[27] Synthesis of porous metal phosphonate hybrid materials represents a vital research direction mainly because of the fact

that the use of organophosphonic acid and the corresponding derivatives provides an almost infinite potential to adjust the organic component in the framework and/or on the surface leading to various modes of functionalization of the hybrid materials.[23,28] Furthermore, the incorporation of porous hierarchy into metal organophosphonates could result in the enhanced properties compared with single-sized pore materials, due to the increased mass transport through the large pore channels of the material and the maintenance of high specific surface area on the level of fine pore systems,[29,30] though hierarchical porous metal phosphonates with well-structured micromorphology were scarcely reported.

Heavy metal ions have caused irreversible damage to the environment and human health. For the removal of heavy metal ions in the waste water, metal phosphonates have shown as candidate adsorbents, which is due to that organic functionalities in the hybrid network typically serve to form complexes with heavy metal ions through acid-base reactions. Mesoporous titania-phosphonate and macroporous titanium phosphonate hybrid materials were successfully synthesized and showed high adsorption capabilities.[31] However, most reported works were focused on the uptake capacities and selectivities of different metal ions, and little interest was casted to the adsorption mechanism for metal phosphonates. On the other hand, biomolecule immobilization and separation play vital roles in the fields of biology, pharmacy and bioengineering. Porous metal phosphonate materials could find their application for biomolecule sorption/immobilization.[29] Although many types of materials including silicas,[32] zeolites,[33] hydrogel polymers,[34] and self-assembled monolayers[35] have been considered as effective protein and enzyme carriers, there is still rare work on the biomolecule separation as to metal phosphonates. Noticeably, novel adsorbents with significant porous properties are crucial to realize and enhance separation efficiency of different biomolecules.[36,37]

In this contribution, a self-templating microemulsion process was reported for the preparation of hollow manganese phosphonate microspheres with hierarchical porous shells. Since the organic bridging groups were homogeneously distributed in the hybrid network, the synthesized manganese phosphonate materials could be used for Cu^{2+} adsorption. The effects of the progress parameters including pH value, temperature and initial Cu^{2+} concentration on the removal capacities were investigated. To better understand the adsorption characteristic, some isotherm and kinetic models were utilized to illustrate the sorption process. Furthermore, the synthesized manganese phosphonate microspheres were utilized to separate cytochrome *C* and protein bovine serum albumin, showing good separation efficiency on the basis of the different size of the two protein molecules.

2. Experimental

2.1 Materials and synthesis

Manganese chloride ($MnCl_2$), $Cu(NO_3)_2$, hydrochloric acid (HCl), and sodium hydroxide (NaOH) were obtained from Tianjin Guangfu Chemical Co. Sodium salt of ethylene diamine tetra(methylene phosphonic acid) (EDTMP) was donated from Henan Qingyuan Chemical Co. Cytochrome *C* (Cyt *C*) and the protein bovine serum albumin (BSA) were obtained from Beijing (China) Dingguo Biotechnology Co. All chemicals were used as received without any further purification.

In a typical synthesis of hollow manganese phosphonate microspheres, 10 ml of EDTMP solution (0.1 mol L^{-1}) was dropwise added into 20 ml of $MnCl_2$ aqueous solution (0.2 mol L^{-1}) under mild stirring, and the final pH was adjusted by 0.1 mol L^{-1} HCl and 0.1 mol L^{-1} NaOH to about 5. After 2 h of stirring, the obtained mixture was transferred into a Teflon-lined autoclave and aged statically at 140 ºC under autogenous pressure for 24 h. The as-synthesized products were filtered, washed by distilled water and ethanol alternatively for several times, and dried at 110 ºC overnight. The resultant material was labeled as HMPM, abbreviated for hollow manganese phosphonate microspheres.

2.2 Characterization

Scanning electron microscopy (SEM) was carried out on a Jeol JSF-7500L at 5 keV. Transmission electron microscopy (TEM) was carried out on a Jeol JEM 2100F at 200 kV. All samples subjected to TEM measurements were ultrasonically dispersed in ethanol and dropcast onto copper grids covered with a carbon film. X-ray diffraction (XRD) patterns were recorded on a Bruker D8 Focus Diffractometer with Cu-Kα radiation (λ = 0.15418 nm) operated at 40 kV and 40 mA. N_2 adsorption-desorption isotherms were measured on a Quantachrome NOVA 2000e sorption analyzer at liquid nitrogen temperature (77 K). The samples were degassed at 110 ºC overnight prior to the measurement. The surface areas were calculated by the multi-point Brunauer-Emmett-Teller (BET) method, the pore size distributions were obtained from the isotherms by the NLDFT (Non-local Density Functional Theory) model. Fourier transform infrared (FT-IR) spectra were measured on a Bruker VECTOR 22 spectrometer with KBr pellet technique, and the ranges of spectrograms were 4000 to 400 cm^{-1}. Simultaneous thermogravimetry (TG) and differential scanning calorimetry (DSC) were performed using a TA SDT Q600 instrument at a heating rate of 5 ºC/min using α-Al_2O_3 as the reference. X-ray photoelectron spectroscopy (XPS) measurements were performed on a Kratos Axis Ultra DLD (delay line detector) spectrometer equipped with a monochromatic Al-Kα X-ray source (1486.6 eV). All XPS spectra were recorded using an aperture slot of 300 × 700 microns, survey spectra were recorded with a pass energy of 160 eV, and high resolution spectra with a pass energy of 40 eV.

2.3 Metal ions adsorption

The isotherm studies for the adsorption of Cu^{2+} ions were tested as follows: 0.01 g of the manganese phosphonate samples were added into 50 ml of $Cu(NO_3)_2$ aqueous solutions with different

concentrations (0.5 – 50 mg L^{-1}). The experiments were performed at different temperature (20, 30, and 40 ºC). The mixture was stirring for 2 h to access the adsorption-desorption balance, followed by centrifugation at 6000 rpm for 15 min. The concentrations of metal ions in the initial and final solutions were monitored through atomic absorption spectroscopy (AAS) analysis. To investigate the kinetic characteristics of the adsorption, 0.01g of HMPM was added into a Cu^{2+} solution of three different concentrations (5, 10, and 50 mg L^{-1}) at pH = 6. After stirring for regular time, the Cu^{2+} loaded HMPM was separated, and the residual concentration of Cu^{2+} in the solution was measured. All the adsorption experiments were carried out at least three times.

2.4 Protein adsorption test

Typically, Cyt *C* and BSA phosphate buffer solutions (PBS, pH = 7.2) with the concentration of 1 mg ml^{-1} were prepared, respectively. Then, 5 ml of the protein solution were mixed with each other and shifted to the vessel containing 50 mg of the HMPM sample, followed by stirring under ambient conditions. The supernatant liquor was separated at a given time interval, and the amount of protein adsorbed was monitored by measuring the UV adsorption at 360 nm for Cyt *C* and 277 nm for BSA, respectively.

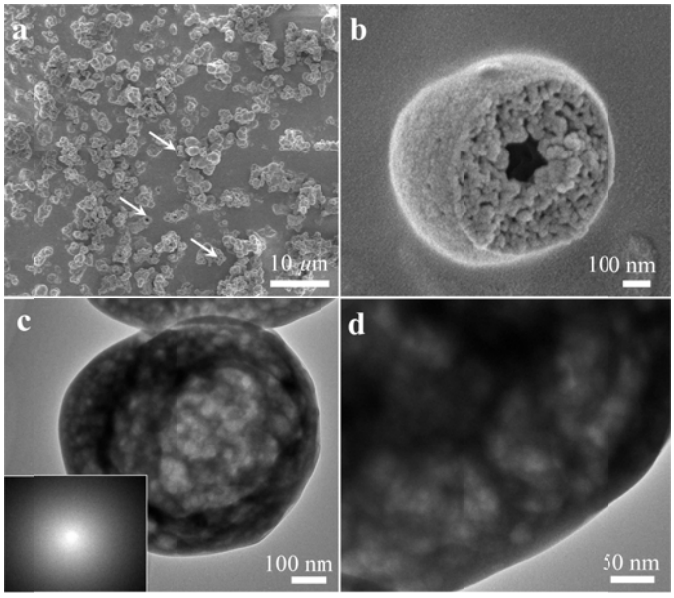

Fig. 1 SEM (a, b) and TEM (c, d) images of HMPM. Hollow spheres emphasized with arrows in (a), and the inset of (c) shows the selected area electron diffraction patterns.

3. Results and discussion

3.1 Material synthesis and characterization

Hollow spherical manganese phosphonates were prepared through a facile template-free route, which involved the addition of the manganese choloride into EDTMP, followed by a hydrothermal process. The micromorphology of the synthesized hybrids was characterized by SEM and TEM. The low-magnification SEM images of hollow manganese phosphonates in Fig. 1a demonstrate well-defined microspheres with high yield. The average diameter of these hybrid microspheres is approximately 0.5 – 2 μm. Besides, these spheres tend to aggregate slightly, which may be attributable to the high surface energy of hollow morphology, and the aggregation may happen primarily during the ripening process.[38] The interior structure is revealed by a single broken sphere (Fig. 1b), and it can be observed that the microspheres possess a hollow interior with a porous shell. The shell thickness is of about 150 nm, which is resulted from the aggregation of nanospherical particles with diameters of 5 – 35 nm. The detailed morphology of the hollow microspheres was further analyzed by TEM micrographs. As shown in Fig. 1 c, the pale center and the relatively dark edge indicate the hollow natures of the hybrid spheres. The shell thickness is around 130 nm, which is almost consistent with the SEM observation. Interestingly, a novel mesocellular foam structure, akin to previously reported silicas with mesostructured cellular foam (MCF),[39] can be seen. Secondary mesostructured pores of several nanometers are emerged near the inferior pore surface layers, revealed by the high-resolution TEM images (Fig. 1d). The hollow phosphonate-based hybrid microspheres with unusual shells of porous hierarchy fabricated in the absence of any templates has been rarely reported. The synthesized HMPM hybrid materials possess amorphous framework shells, as revealed by the selected area electron diffraction pattern (inset of Fig. 1c) and wide-angle XRD patterns (Fig. S1, ESI).

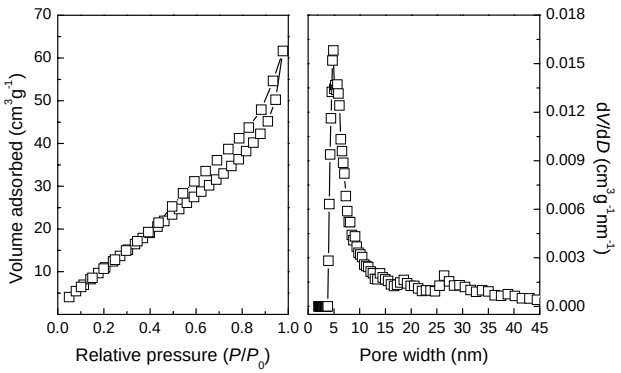

Fig. 2 N_2 adsorption-desorption isotherms (left) and the corresponding pore size distribution curve (right) of the HMPM.

The N_2 adsorption-desorption isotherm and the corresponding pore size distribution curve of the HMPM are shown in Fig. 2. The sorption isotherm is of between type II and type IV, which is characteristic of mesoporous structures with fine pore connectivity.[40] The nitrogen volume adsorbed rises steeply at high relative pressure (P/P_0 > 0.8) and do not level off, indicating the presence of an appreciable amount of secondary porosity of large pores. The pore size distribution estimated by NLDFT model exhibits a narrow peak in the range of 4 – 12 nm and the other relatively broad distribution at 16 – 30 nm. These two kinds of mesopore size distributions are attributed to the mesostructured pores in the shell surface

sections and the interior mesocellular foam structure of the amorphous shells, respectively. The BET surface area and pore volume are 66 m^2 g^{-1} and 0.095 cm^3 g^{-1}, respectively.

Instead of employing typical emulsion-templating methods with nonpolar solvents such as trimethylbenzene, a self-templating emulsion route for the formation of spherically shaped hollow phosphonate-based hybrid with hierarchically porous shells can be assumed. A possible formation mechanism is depicted in Fig. 3. It could be considered that drops of liquid organophosphonic claw molecules added to manganese choloride solution did not disappear immediately but, on the contrary, the drops broke up into many smaller nanosized spheres under mild stirring, and emulsion-like solution was thus generated. The phosphonic droplets became covered with the subsequently growing layers of the manganese phosphonates, which could preserve the initial shape of the nanodrops. Upon heating under hydrothermal conditions, a portion of phosphonic droplets gradually defused out through the formed phosphonate shell to react with the remaining inorganic metal precursors in the mixed solution, and this process was similar to the Kirkendall effect.[41] The continuous supply of phosphonic acid and metal ions exerted a thermodynamic control over the condensation between the inorganic units and the organic moieties. Correspondingly, hollow manganese phosphonate mcirospheres possessing mesocelullar foam structures close to the internal shell and secondary smaller mesostructured pores approaching to the surface layers were formed. The progress that resulted in the formation of phosphonate hybrid microspheres is reminiscent of the interfacial emulsion polymerization technique that has been developed for the nanoscaled silver hollow spheres (using *n*-dodecane/water emulsion) and silica (using an oil/water emulsion) hollow nanosphere synthesis.[42,43]

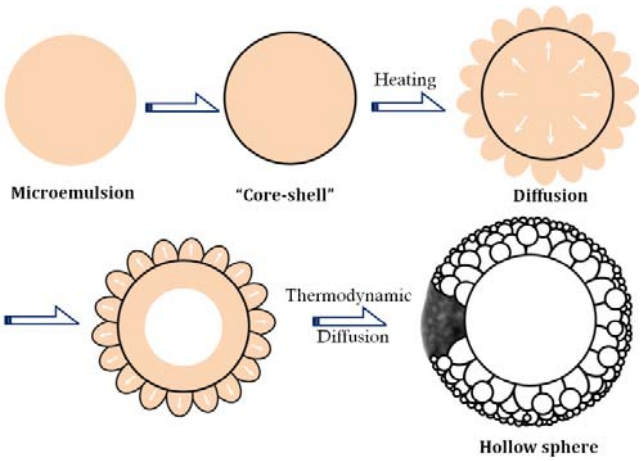

Fig. 3 Possible formation process of the hollow manganese phosphoante hybrid with hierarchially porous shells.

The thermal stability of the manganese hybrid was determined by TG-DSC analysis. The TGA curve (Fig. S2) exhibits an initial weight loss of 8.6% from room temperature to 180 ºC, accompanied with an endothermal peak at 75 ºC in the DSC curve, which can be assigned to the desorption of adsorbed and intercalated water molecules. The decomposition of the organic component of the hybrid framework, mainly due to the carbon and hydrogen atoms exclusion in the form of CO_2 and H_2O, starts at about 180 ºC, resulting in 11.7% weight loss. The skeletal structure and surface chemistry of the synthesized samples were investigated by the FT-IR and X-ray photoelectron spectroscopy. The FT-IR of manganese phosphonates and bridging molecule EDTMP between 4000 and 400 cm^{-1} are given in Fig. S3. The strong broad band around 3400 cm^{-1} and the sharp band at 1638 cm^{-1} correspond to the surface-adsorbed water and hydroxyl groups. The band situated at 573 cm^{-1} can be assigned to stretching vibration of Mn-O bond. The strong band at 1089 cm^{-1} is due to phosphonate P-O···Mn stretching vibrations, and the neighbor weak band at 991 cm^{-1} can be attributed to the defective P-OH.[44] The signal present at 754 cm^{-1} suggests the presence of P-O-P bending modes.[26] The band at 1438 cm^{-1} is due to P-C stretching vibrations. The weak shoulder band at 1323 cm^{-1} is attributed to C-N stretching, while the band attributed to phosphoryl (P=O) frequency at around 1360 cm^{-1} cannot be seen, indicating the complete condensation with manganese centers. In addition, weak bands around 2800-3000 cm^{-1} and the band at 1438 cm^{-1} are assigned to the C-H stretching modes resulting from the methylene and ethylene groups in the organic coupling components.

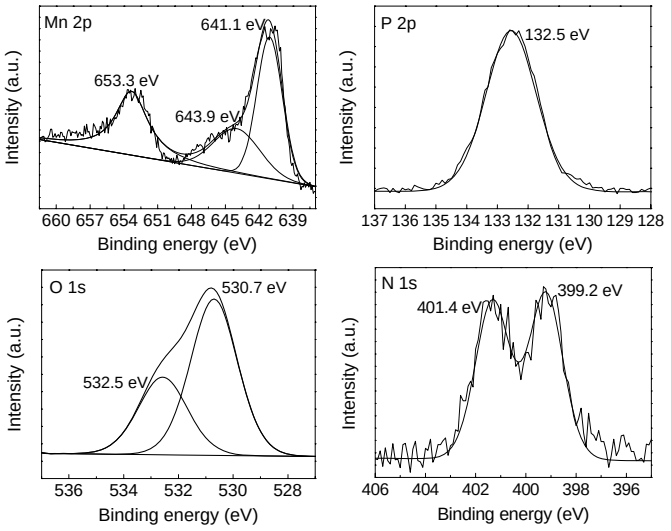

Fig. 4 High-resolution XPS spectrum of the Mn 2p, P 2p, O 1s, and N 1s of the HMPM material.

High-resolution XPS spectrum was taken on the surface of the HMPM sample for the investigation of chemical state (Fig. 4). The binding energies of Mn 2p are found to be 653.3 eV for $2p_{1/2}$ and 641.1 eV for Mn Mn $2p_{3/2}$, respectively. Compared with the binding energy with pure Mn_2O_3 (641.8 eV for Mn $2p_{3/2}$ and 653.4 eV for Mn $2P_{1/2}$), the binding energy of the main Mn 2p decreases in the manganese phosphonate hybrid,[45,46] which may be the result from the organophosphonate incorporation in the network. The Mn $2p_{3/2}$

are found to be broad, presenting a shoulder at 643.9 eV, which indicates the existence of higher valent Mn species.[47] One symmetrical peak of the P 2p spectrum for HMPM is observed at 132.5 eV, which is characteristic of P^{5+} in organophosphonate groups. The O 1s lines can be deconvoluted into two components, revealing two kinds of oxygen species. The broad signal at 529.4 eV can be ascribed to the bridging oxygen in the P-O···Mn linkages, and a shoulder around 532.5 eV can correspond to the surface hydroxyl. The N 1s spectrum shows a component at 399.2 eV accompanied with the other one at 401.4 eV, corresponding to bridged N-containing compounds.

3.2 Heavy metal ion adsorption

Since the synthesized manganese phosphonate materials contain alternative organic functional moieties in the framework, which can contribute coordination interactions with metal ions, the phosphonate hybrids can perform as efficient adsorbents for the metal ion removal from water, and thus their corresponding adsorption performances, exemplified by Cu^{2+} ions, were studied. The pH value of the aqueous solution is an important parameter that influences the adsorption behaviors. The adsorption experiments were carried out in the pH range of 2 – 8, and the adsorption efficiency is presented in Fig. 5. The removal efficiency increases from pH = 2 to 6. This result can be attributed to the protonation of the donating nitrogen atoms in the phosphonic bridging groups under acidic condition,[48] which impairs the chelation ability of the ethylene diamine groups with Cu^{2+}. When the pH value was further adjusted to weakly alkaline conditions, the Cu^{2+} could form the precipitate of copper hydroxide. In order to ensure the accuracy of quantitative adsorption and avoid the hydrolysis of Cu^{2+}, an optimal pH of 6 is selected for the following adsorption tests.

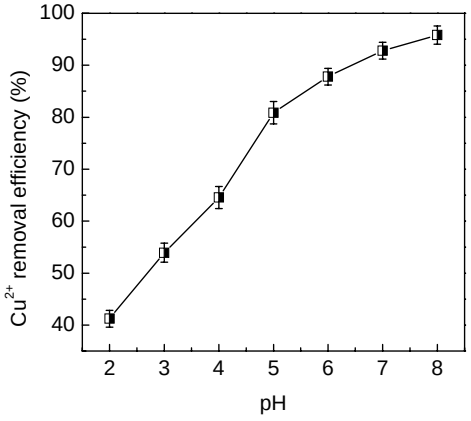

Fig. 5 The percentage Cu^{2+} removed by the synthesized HMPM hybrid under different pH conditions (treated with a 20 mg L^{-1} $Cu(NO_3)_2$ solution).

Adsorption isotherm studies are of fundamental significance in designing sorption systems since they reflect how the adsorbates partitioned between the solid adsorbents and liquid phases at equilibrium as a function of the concentration. In this work, Langmuir, Freundlich and Temkin models were used to investigate the adsorption equilibrium between manganese phosphonates and Cu^{2+}. The Langmuir model assumes a monolayer adsorption on a homogeneous surface without any interaction between the adsorbed molecules,[49] and the corresponding linearized equation can be presented as:

$$C_e/q_e = C_e/q_{max} + 1/K_L q_{max} \quad (1)$$

where q_e (mg g^{-1}) and C_e (mg L^{-1}) are the adsorption capacity and the equilibrium concentration of the adsorbate, respectively, q_{max} (mg g^{-1}) is the maximum adsorption capacity of adsorbents, while K_L (L mg^{-1}) is a constant related to the affinity of the binding sites.

Different from the Langmuir isotherm model, Freundlich isotherm expresses adsorption in a multilayer manner on energetically heterogeneous surface which can be expressed as:[50]

$$\log q_e = \log K_F + 1/n \log C_e \quad (2)$$

where K_F and n are the Freundlich constants that are related to adsorption capacity and intensity, respectively.

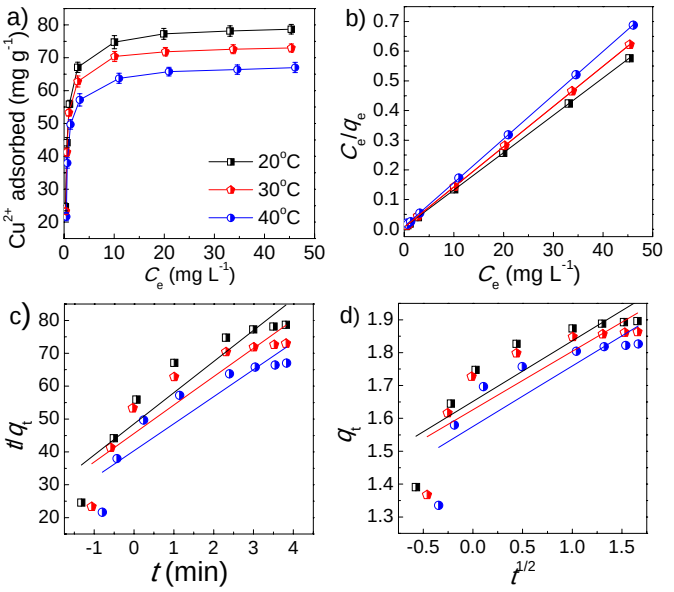

Fig. 6 Adsorption isotherms for the HMPM adsorbent measured at 20, 30 and 40 ºC, respectively (a). Langmuir (b), Freundlich (c) and Temkin (d) isotherms for the adsorption of Cu^{2+}.

The derivation of the Temkin isotherm is based on the assumption that the decline of the heat of sorption as a function of temperature is linear rather than logarithmic, as implied in the Freundlich equation.[51] It can be described as follows:

$$q_e = \frac{RT}{b_T} \ln a_T + \frac{RT}{b_T} \ln C_e \quad (3)$$

where a_T (L g^{-1}) is the equilibrium binding constant corresponding to the maximum binding energy, b_T (kJ mol^{-1}) is the Temkin constant related to the heat of sorption, and R is the gas constant, T is the absolute temperature (K). All the isotherm constants were determined by the linear regression (Fig. 6) and summarized in Table 1. It is evident that the value of the correlation coefficient (R^2) estimated from the Langmuir model is considerably higher than that estimated from Freundlich or

Table 1 Adsorption equilibrium parameterss calculated from Langmuir, Freundlich and Temkin models in the adsorption of Cu^{2+} onto HMPM.

Temperature	Langmuir			Freundlich			Temkin		
/ºC	q_{max} /mg g^{-1}	K_L /L mg^{-1}	R^2	n	K_F	R^2	a_T /L g^{-1}	b_T /kJ mol^{-1}	R^2
20	79.5	1.96	0.999	5.43	5.21	0.881	166	0.239	0.879
30	73.7	1.86	0.999	5.62	5.08	0.852	194	0.291	0.837
40	67.9	1.65	0.999	5.42	4.83	0.851	134	0.316	0.839

Temkin model, implying that the adsorption of copper ions by manganese phosphonates was a monolayer adsorption process. The maximal adsorption capacity according to the Langmuir equation is calculated to be 79.5, 73.7 and 67.9 mg g^{-1} at 20, 30 and 40 ºC, respectively.

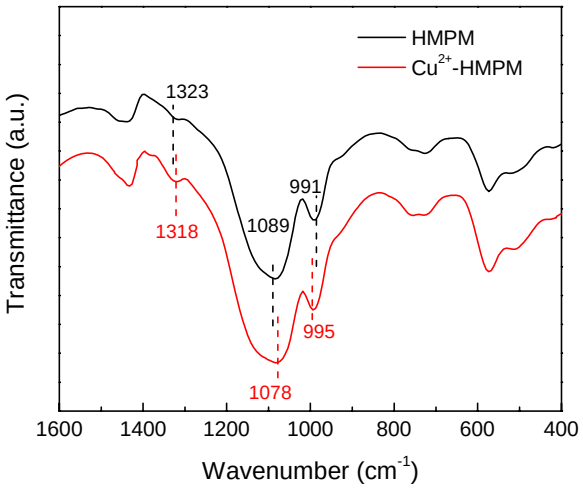

Fig. 7 FT-IR spectrum of HMPM and the Cu^{2+} loaded HMPM.

The FT-IR spectrum of Cu^{2+} chelated HMPM also confirmed the coordination of Cu^{2+} on the hybrid hollow spheres (Fig. 7). The C-N stretching vibrations were observed at 1318 cm^{-1}, P-OH vibrations at 995 cm^{-1} and P-O···Mn stretching mode at 1078 cm^{-1}, showing a slight shift as compared to HMPM: -5 cm^{-1}, -11 cm^{-1} and +4 cm^{-1} respectively, which were caused by the coordination interactions between the Cu^{2+} and EDTMP linkages in the hybrid framework. The HMPM hybrid before and after Cu^{2+} adsorption were further characterized by UV-vis diffuse-reflectance spectrum (Fig. S4). The Cu^{2+}-loaded HMPM sample shows an additional broad absorbance ranging from 600 to 800 nm. This phenomenon can be related to the Cu-EDTMP complex on the surface of the hybrid materials,[26] similar to the coordination effect of the ethylenediamine-functionalized porous silica systems.[52,53] So, the resultant high adsorption ability of the inorganic-organic manganese phosphonate hybrids is mainly resulted from the bridging phosphonic linkers containing ligands for binding metal, including the pyridinic nitrogen atoms, bridging hydrocarbon chains and incompletedly condensed P-OH groups.[54] Furthermore, both q_{max} and K_L decreased with the increase of the temperature, suggesting that the interaction between Cu^{2+} and the inorganic-organic adsorbent weakened at higher temperature and the adsorption process was exothermic. However, the binding abilities of HMPM are found to be much higher than previously reported Cu^{2+}-imprinted mesoporous silica adsorbents with high surface area of 1203 m^2 g^{-1} (24.8 mg g^{-1}) and mesoporous hydroxyethylidene-bridged diphosphonic modified titania with surface area of 257 m^2 g^{-1} (28.8 mg g^{-1}).[55,56] The heavy metal ion adsorption results indicated that not only the specific surface area but also the variety of the organophosphonic bridging groups condensed with hybrid framework was responsible for the improvement of ion binding capacities. The formation of chelating complexes due to the coordination metal ions with uncondensed P-OH and pyridinic nitrogens could be of great benefit to the high ion adsorption capacities.

Cu^{2+} aqueous solutions of three different initial concentrations were employed to investigate the adsorption kinetics of Cu^{2+} on the manganese phosphonate adsorbent at 30 ºC. The experimental results (Fig. 8a) exhibit that the adsorption rate is rapid. The equilibrium adsorption time tend to prolong as the Cu^{2+} concentration increases. And, the maxima uptake can be reached within 20, 25, and 32 min for 5, 10, and 50 mg L^{-1} initial solution concentrations, respectively. The equilibrium adsorption time is much faster than that of diamine modified mesoporous silica (> 60 min).[57] The fast adsorption equilibrium may be resulted from the well-defined hierarchical porosity across the shells of manganese phosphonate microspheres, which could improve the mass transfer and facilitate the metal ion diffusion through the porous spheres. To illustrate the mechanism of adsorption and determine the rate-controlling steps including mass transport and chemical reaction processes during the adsorption process, several kinetic models such as pseudo-first order, pseudo-second order and intraparticle diffusion models were used to simulate the adsorption data. Assuming pseudo-first order kinetics, the rate of adsorptive interactions can be evaluated by the Lagergren equation:[58]

$$\ln(q_e - q_t) = \ln q_e - k_1 t \quad (4)$$

where q_e and q_t (mg g^{-1}) represent the adsorbed amounts of Cu^{2+} on HMPM at equilibrium and time t, respectively, and k_1 (min^{-1}) stands for the rate constant of first order adsorption. The pseudo-second order kinetic model is expressed as:[59]

$$t/q_t = 1/k_2 q_e^2 + (1/q_e)t \quad (5)$$

where k_2 (g mg^{-1} min^{-1}) is the second order rate constant and q_e (mg g^{-1}) is the uptake capability calculated by the second order kinetic model. The initial adsorption rate h can be obtained as well based on the following equation:

$$h = k_2 q_e^2 \quad (6)$$

Table 2 Kinetics parameters for the adsorption of Cu^{2+} on the HMPM adsorbent.

C_0[a]	$q_{e,exp}$	Pseudo-first order			Pseudo-second order				Intraparticle diffusion		
		k_1	R^2	q_e	k_2	h	q_e	R^2	$K_{id,1}$	Intercepts	R^2
5	24.5	1.15	0.924	104.6	0.0253	16.2	25.3	0.999	6.16	-0.369	0.996
10	49.7	1.12	0.962	210.6	0.0310	32.2	50.6	0.999	12.2	-0.358	0.998
50	74.5	0.940	0.906	267.7	0.024	36.3	76.2	0.999	16.0	1.64	0.996

[a] Initial Cu^{2+} concentrations.

Fig. 8 shows the linearized forms for the sorption of Cu^{2+} onto manganese phosphonates calculated by pseudo-first and second order equations at various initial concentrations, and the fitted results are tabulated in Table 2. The theoretical q_e values calculated by first order kinetics model exhibit relatively large deviations compared with the experimental results, and thus the adsorption process cannot be attributed to first order. This may be due to that there is a time lag, which is resulted from a boundary layer or external resistance controlling at the beginning of the sorption.[53] However, according to Fig. 8 and Table 2, it can be found that pseudo-second order model is well fitted with the experimental data since the calculated q_e was considerably close to the experimental, and the correlation coefficients were larger than 0.995, suggesting that the rate-limiting step in adsorption process of heavy metal ions are chemisorption involving valence forces through the sharing or exchange of electrons between adsorbent and metal ions.[60]

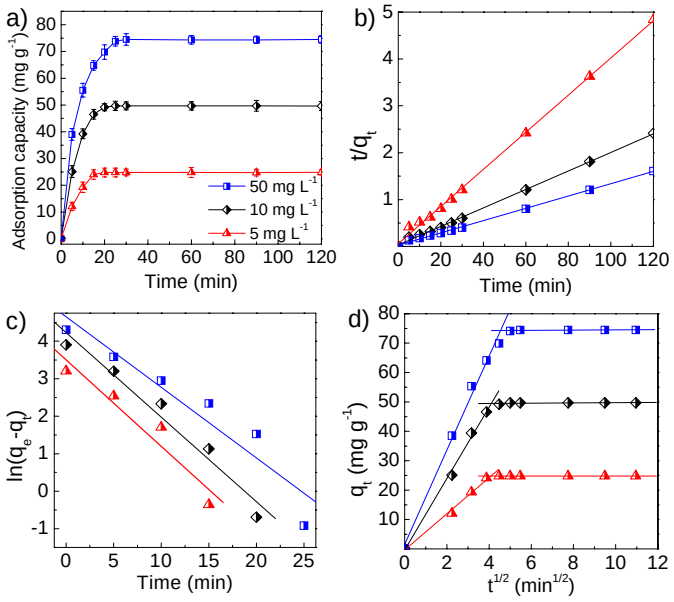

Fig. 8 Effect of contact time on the Cu^{2+} removal (a). Pseudo-first order (b), pseudo-second order (c), and intraparticle diffusion (d) kinetics of Cu^{2+} onto the HMPM hybrid at various initial concertations.

The adsorption of metal ions on a porous adsorbent usually involves a multi-step process: (i) mass transfer from the bulk solution to the boundary layer surrounding the surface of the adsorbent surface; (ii) solute transport from the boundary layer to the surface; (iii) solute transfer from the adsorbent's surface to active intraparticular sites; and (iv) interactions between the solute molecules and the available adsorption sites on the internal surfaces of the adsorbent. The first and second steps were very slow and were assumed to be rate-determining steps. To evaluate how the diffusion affected the adsorption rate, the intraparticle diffusion model was carried out as follows:[61]

$$q_t = k_{id}t^{1/2} + C \quad (7)$$

where k_{id} (mmol g^{-1} $min^{-1/2}$) is the rate constant of the intraparticle diffusion and C represents the thickness of the boundary layer. Fig. 8d demonstrates the multi-linearity of the plot of q_t versus $t^{1/2}$, indicating that multi-step diffusion occurred during the adsorption process. The first slopes can be attributed to the external mass transfer and the second stage is related to the final adsorption equilibrium. Moreover, the deviation of these lines from the origin (a y-intercept other than 0) reveals that the intraparticle diffusion may not be the controlling factor in determining the kinetics of the adsorption process. It is likely that a number of copper ions diffused into the pores before being adsorbed. This may be the result of the well-structured hierarchical porosity that can effectively impair the influence of diffusion process.

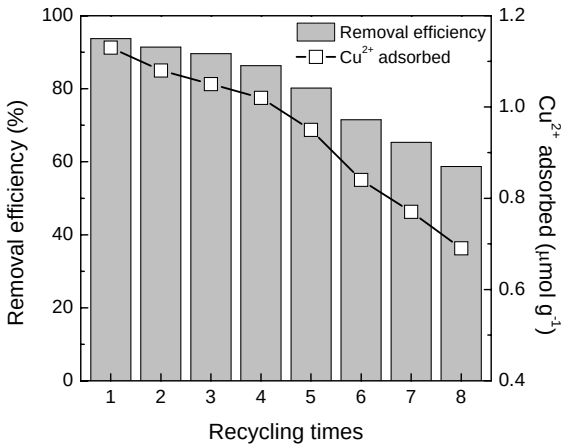

Fig. 9 Reusability of the HMPM adsorbent for Cu^{2+} (initial concentration: 20 mg L^{-1}).

To test the reusability of HMPM adsorbent, the Cu^{2+} ion loaded sample was treated with 1 mol L^{-1} hydrochloric acid for 3 h to remove the heavy metal ions and then neutralized, following a second round of metal ion adsorption testing (20 mg L^{-1} of Cu^{2+}). The results for Cu^{2+} adsorption using the regenerated adsorbents are summarized in Fig. 9. Only a little deteriation of the adsorption capacity (91.4 %) can be observed during the second use, and the sample retained Cu^{2+} removal efficiency of 89.6 % after three times cycles. Then the Cu^{2+} uptake capacities decreased gradually in the next successive

uses, but the hybrid still reserve 62.3 % of the initial metal ion loading capacity after leaching eight times. This suggests the stability of the synthesized hierarchically porous manganese phosphonate materials and the retention of their adsorption properties under the relatively strong acid leaching conditions, making them useful as reusable sorbents for multiple metal ion adsorption cycles.

3.3 Protein separation

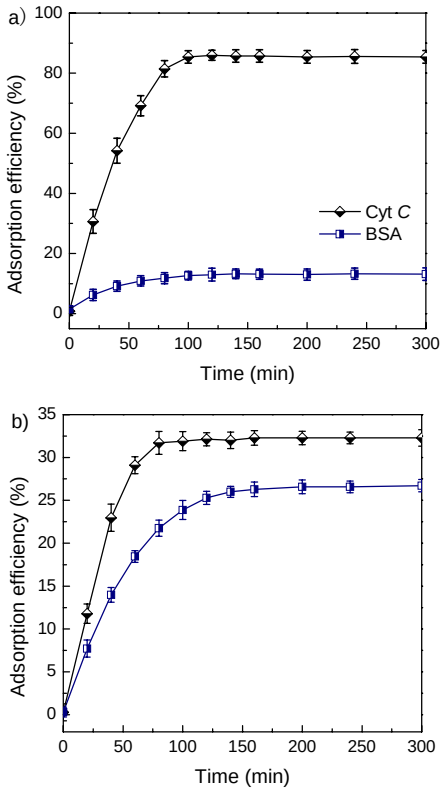

Fig. 10 Time-dependent adsorption curves of Cyt *C* and BSA for the pristine HMPM (a) and the HMPM material after a ball-milling treatment (b).

The controllable adsorption and separation of proteins are indispensable for the application of biosensors, biocatalysts and disease diagnostics. Size-selective adsorption of guest protein molecules, which mainly depends on the porous properties of sorbents, has attracted tremendous research interest due to the feasibility to adjust the porosity of the host solid materials. Although usual porous sorbents have good capacities toward adsorbates, they still confront with the predicament in separating proteins from each other. In this study, Cyt *C* (12 400 Da, 2.6 × 3.2 × 3.3 nm^3) and BSA with a relatively larger size (66 400 Da, 5.0 × 7.0 × 7.0 nm^3) are chosen as the probe proteins. The result of simultaneous adsorption on manganese phosphonate spherical hybrid is shown in Fig. 10a. Cyt C adsorption increases sharply at the initial contact time and slows down gradually until adsorption equilibrium is reached, demonstrating an adsorption efficiency of 85.7 %. On the contrary, the HMPM hybrid shows much lower adsorption capability for BSA (13.1 %). This may be resulted from the porous hierarchy of HMPM. Since mesostructured pores with small pore size were distributed in the shell sections of manganese phosphonate microspheres, which would permit the penetration of small molecules (Cyt *C*) through the adsorbent and block BSA molecules with larger size. Thus, the analogous "semipermeable membrane" effect would favor the separation of proteins with different sizes. Noticeably, the microspherical morphology with porous hierarchy was destroyed by a ball-milling technique before adsorbing proteins, leading to a little decrease of specific surface area to 48 m^2 g^{-1} and a wide pore size distribution from 0 to 40 nm (Fig. S5 and S6). As seen in Fig. 10b, both the protein molecules can be adsorbed and the separation goal cannot be achieved. Moreover, the resultant adsorption ability for Cyt *C* is much lower than that of HMPM, which may be due to the existence of competitive adsorption of the two proteins on the sorbent surface. Therefore, such a good selectivity is mainly attributable to the peculiar porosity of the manganese phosphonate microspheres.

4. Conclusions

Hollow manganese phosphonate microspheres with hierarchically porous shells have been synthesized through a template-free method. The inorganic-organic manganese phosphonate hybrids possess an amorphous framework with homogeneous intraframework organic functional groups that perform as binding sites for heavy metal ion adsorption. The resultant hybrids show fast adsorption kinetics, which is due to that the well-defined porous structure could enhance mass transfer through the bulk microspheres. The unique porous hierarchy through the phosphonate microspheres endowed the hybrid with excellent size selectivity for the adsorption in the mixed protein solution of BSA and Cyt *C*. The synthesis method is facile and the results of this methodological study are applicable for the removal and recovery of heavy metal ions during water environment pollution treatment and the bioapplications such as diagnosis, drug delivery, and disease-relevant biomarker screening.

Acknowledgements

This work was supported by the National Natural Science Foundation of China (21076056 and 21073099), the Specialized Research Fund for the Doctoral Program of Higher Education (20110031110016), the Program for Innovative Research Team in University (IRT13022), the 111 project (B12015), and the Key Laboratory of Advanced Catalytic Materials in Zhejiang Normal University (ZJHX201301).

Notes and references

[a] Key Laboratory of Advanced Energy Materials Chemistry (Ministry of Education), Collaborative Innovation Center of Chemical Science and Engineering (Tianjin), College of Chemistry, Nankai University, Tianjin 300071, China. E-mail: zyyuan@nankai.edu.cn.

[b] School of Chemical Engineering and Technology, Hebei University of Technology, Tianjin 300130, China.

† Electronic Supplementary Information (ESI) available. See DOI: 10.1039/b000000x/

1 M. W. Zhao, Y. N. Gao, L. Q. Zheng, W. P. Kang, X. T. Bai and B. Dong, *Eur. J. Inorg. Chem.*, 2010, 975–982.
2 J. Du, J. Qi, D. Wang and Z. Y. Tang, *Energy Environ. Sci.*, 2012, **5**, 6914–6918.
3 X. Y. Lai, J. E. Halperta and D Wang, *Energy Environ. Sci.*, 2012, **5**, 5604–5618.
4 M. Y. Liao, C. C. Huang, M. C. Chang, S. F. Lin, T. Y. Liu, C. H. Su, C. S. Yeh and H. P. Lin, *J. Mater. Chem.*, 2011, **21**, 7974–7981.
5 A. D. Dinsmore, M. F. Hsu, M. G. Nikolaides, M. Marquez, A. R. Bausch and D. A. Weitz, *Science*, 2002, **298**, 1006–1009.
6 H. P. Cong and S. H. Yu, *Adv. Funct. Mater.*, 2007, **17**, 1814–1820.
7 J. Li, X. Y. Lai, C. J. Xing and D. Wang, *J. Nanosci. Nanotech.*, 2010, **10**, 7707–7710.
8 X. Y. Lai, J. Li1, B. A. Korgel, Z. H. Dong, Z. M. Li, F. B. Su, J. Du and D. Wang, *Angew. Chem. Int. Ed.*, 2011, **50**, 2738–2741.
9 S. Soll, T. P. Fellinger, X. C. Wang, Q. Zhao, M. Antonietti and J. Y. Yuan, *Small*, 2013, **9**, 4135–4141.
10 S. W. Song, K. Hidajat and S. Kawi, *Langmuir*, 2005, **21**, 9568–9575.
11 R. H. Zhu, X. Y. Lai, J. E. Halpert, R. B. Yu and D. Wang, *Eur. J. Inorg. Chem.*, 2012, 2665–266.
12 X. B. Li, Y. Yang and Q. H. Yang, *J. Mater. Chem. A*, 2013, **1**, 1525–1535.
13 M. K. Park, K. Onishi, J. Locklin, F. Caruso and R. C. Advincula, *Langmuir*, 2003, **19**, 8550–8554.
14 S. W. Kim, M. Kim, W. Y. Lee and T. Hyeon, *J. Am. Chem. Soc.*, 2002, **124**, 7642–7643.
15 D. H. W. Hubert, M. Jung, P. M. Frederik, P. H. H. Bomans, J. Meuldijk and A. L. German, *Adv. Mater.*, 2000, **12**, 1286–1290.
16 Y. R. Ma, J. M. Ma and H. M. Cheng, *Langmuir*, 2003, **9**, 4040–4042.
17 C. I. Zoldesi and A. Imhof, *Adv. Mater.*, 2005, **17**, 924–928.
18 Y. D. Yin, R. M. Rioux, C. K. Erdonmez, S. Hughes, G. A. Somorjaiand and A. P. Alivisatos, *Science*, 2004, **304**, 711–714.
19 X. W. Lou, Y. Wang, C. Yuan, J. Y. Lee and L. A. Archer, *Adv. Mater.*, 2006, **18**, 2325–2329.
20 J. G. Yu, H. T. Guo, S. A. Davis and S. Mann, *Adv. Funct. Mater.*, 2006, **16**, 2035–2041.
21 C. H. An, J. Z. Wang, J. X. Liu, S. T. Wang and Y. G. Sun, ChemSusChem, 2013, 6, 1931–1937.
22 H. J. Hah, J. S. Kim, B. J. Jeon, S. M. Koo and Y. E. Lee, *Chem. Commun.*, 2003, 1712–1713.
23 T. Y. Ma and Z. Y. Yuan, *ChemSusChem*, 2011, **4**, 1407–1419.
24 A. Dutta, A. K. Patra, H. Uyama and A. Bhaumik, ACS Appl. Mater. Interfaces, 2013, 5, 9913–9917.
25 T. Kimura, *Chem. Mater.*, 2005, **17**, 337–344.
26 T. Y. Ma, X. Z. Lin and Z. Y. Yuan *J. Mater. Chem.*, 2010, **20**, 7406–7415.
27 Y. P. Zhu, T. Z. Ren and Z. Y. Yuan, *New J. Chem.*, 2014, DOI: 10.1039/c3nj01139a
28 G. K. H. Shimizu, R. Vaidhyanathan and J. M. Taylor, *Chem. Soc. Rev.*, 2009, **38**, 1430–1449.
29 T. Y. Ma, X. J. Zhang and Z. Y. Yuan, *J. Phys. Chem. C* **2009**, *113*, 12854–12862.
30 Z. Y. Yuan and B. L. Su, *J. Mater. Chem.*, 2006, **18**, 663–677.
31 T. Y. Ma, X. J. Zhang, G. S. Shao, J. L. Cao and Z. Y. Yuan, *J. Phys. Chem. C*, 2008, **112**, 3090–3096.
32 S. E. Létant, B. R. Hart, S. R. Kane, M. Z. Hadi, S. J. Shields and J. G. Reynolds, *Adv. Mater.*, 2004, **16**, 689–693.
33 J. M. Wu, X. Li, Y. E. Yan, Y. Y. Hu, Y. H. Zhang and Y. Tang, *J. Colloid Interf. Sci.*, 2013, **406**, 130–138.
34 R. Huang and N. F. Hu, *Biophys. Chem.*, 2003, **104**, 199–208.
35 X. Chen, R. Ferrigno, J. Yang and G. M. Whitesides, *Langmuir*, 2002, **18**, 7009–7015.
36 M. Zhang, Y. Wu, X. Feng, X. He, L. Chen and Y. Zhang, *J. Mater. Chem.*, 2010, **20**, 5835–5842.
37 B. W. Davis, N. Niamnont, C. D. Hare, M. Sukwattanasinitt and Q. Cheng, *ACS Appl. Mater. Interfaces*, 2010, **2**, 1798–1803.
38 H. P. Hentze, S. R. Raghavan, C. A. Mckelvey and E. W. Kaler, *Langmuir*, 2003, **19**, 1069–1074.
39 Q. Li, Z. X. Wu, D. Feng, B. Tu and D. Y. Zhao, *J. Phys. Chem. C*, 2010, **114**, 5012–5019.
40 T. Y. Ma, X. J. Zhang and Z. Y. Yuan, *Micropor. Mesopor. Mater.*, 2009, **123**, 234–242.
41 A. Cabot, M. Ibáñez, P. Guardia and A. P. Alivisatos, *J. Am. Chem. Soc.*, 2009, **131**, 11326–11328.
42 C. Kind, R. Popescu, E. Müller and C. Feldmann, *Nanoscale*, 2010, **2**, 2223–2229.
43 S. Schacht, Q. Huo, I. G. Voigt-Martin, G. D. Stucky and F. Schuth, *Science*, 1996, **273**, 768–771.
44 M. Vasylyev and R. Neumann, *Chem. Mater.*, 2006, **18**, 2781–2783.
45 Y. Zhang, B. S. Liu, F. M. Zhang and Z. F. Zhang, *J. Hazard. Mater.*, 2013, **15**, 81–88.
46 Y. F. Qu, J. X. Guo, Y. H. Chu, M. C. Sun and H. Q. Ying, *Appl. Surf. Sci.*, 2013, **282**, 425–431.
47 E. Park, M. Kim, H. Jung, S. M. Chin and J. Jurng, *ACS Catal.*, 2013, **3**, 1518–1525.
48 X. Shi, J. P. Li, Y. Tang and Q. H. Yang, *J. Mater. Chem.*, 2010, **20**, 6495–6504.
49 A. El-Sikaily, A. E. Nemr, A. Khaled and O. Abdelwehab, *J. Hazard. Mater.*, 2007, **148**, 216–228.
50 S. Y. Liu, J. Gao, Y. J. Yang, Y. C. Yang and Z. X. Ye, *J. Hazard. Mater.*, 2010, **173**, 558–562.
51 F. P. Zhao, E. Repo, D. L. Yin and M. E. T. Sillanpää, *J. Colloid Interf. Sci.*, 2013, **409**, 174–182.
52 K. Z. Hossain and L. Mercier, *Adv. Mater.*, 2002, **14**, 1053–1056.
53 S. Dai, M. C. Burleigh, Y. Shin, C. C. Morrow, C. E. Barnes and Z. Xue, *Angew. Chem., Int. Ed.*, 1999, **38**, 1235–1239.
54 T. Y. Ma, X. Z. Lin, X. J. Zhang and Z. Y. Yuan, *New J. Chem.*, 2010, **34**, 1209–1216.
55 C. C. Kang, W. M. Li, L. Tan, H. Li, C. H. Wei and Y. W. Tang, *J. Mater. Chem. A*, 2013, **1**, 7147–7153.
56 X. J. Zhang, T. Y. Ma and Z. Y. Yuan, *Eur. J. Inorg. Chem.*, 2008, 2721–2726.
57 W. J. Yang, P. Ding, L. Zhou, J. G. Yu, X. Q. Chen and F. P. Jiao, *Appl. Surf. Sci.*, 2013, **282**, 38–45.
58 W. S. W. Ngah and S. Fatinathan, *Chem. Eng. J.*, 2008, **143**, 62–72.
59 Q. Cao and F. Huang, Z. Y. Zhuang and Z. Lin, *Nanoscale*, 2012, **4**, 2423–2430.
60 X. J. Hu, J. S. Wang, Y. G. Liu, X. Li, G. M. Zeng, Z. L. Bao, X. X. Zeng, A. W. Chen and F. Long, *J. Hazard. Mater.*, 2011, **185**, 306–314.

61 D. B. Wu, Y. H. Sun and Q. G. Wang, *J. Hazard. Mater.*, 2013, **260**, 409–419.

